Crustal Structure of the UAE-Oman Mountain Range and Arabian Rifted Passive Margin: New Constraints From Active and Passive Seismic Methods

S. Pilia[1] , **M. Y. Ali[2]** , **M. P. Searle[3]** , **A. B. Watts[3]** , **C. Lü[1]** , and **D. A. Thompson[4,5]**

[1]Department of Earth Sciences-Bullard Labs, University of Cambridge, Cambridge, UK, [2]Department of Earth Sciences, Khalifa University of Science and Technology, Abu Dhabi, UAE, [3]Department of Earth Sciences, University of Oxford, Oxford, UK, [4]School of Earth and Ocean Sciences, Cardiff University, Cardiff, UK, [5]Now at Omanos Analytics, Glasgow, UK

Abstract The Semail ophiolite, a thick thrust sheet of Late Cretaceous oceanic crust and upper mantle, was obducted onto the previously rifted Arabian continental margin in the Late Cretaceous, and now forms part of the United Arab Emirates (UAE)-Oman mountain belt. A deep foreland basin along the west and SW margin of the mountains developed during the obduction process, as a result of flexure due to loading of the ophiolite and underlying thrust sheets. The nature of the crust beneath the deep sedimentary basins that flank the mountain belt, and the extent to which the Arabian continental crust has thickened due to the obduction process are outstanding questions. We use a combination of active- and passive-source seismic data to constrain the stratigraphy, velocity structure and crustal thickness beneath the UAE-Oman mountains and its bounding basins. Depth-migrated multichannel seismic reflection profile data are integrated in the modeling of traveltimes from long offset reflections and refractions, which are used to resolve the crustal thickness and velocity structure along two E-W onshore/offshore transects in the UAE. Additionally, we apply the virtual deep seismic sounding method to distant earthquake data recorded along the two transects to image crustal thickness variations. Active seismic methods define the Semail ophiolite as a high-velocity body dipping to the east at 40°–45°. The new crustal thickness model presented in this work provides evidence that a crustal root is present beneath the Semail ophiolite, suggesting that folding and thrusting during the obduction process may have thickened the pre-existing crust by 16 km.

1. Introduction

The complex structure and rocks of the UAE-Oman mountain belt (Figure 1) have been crucial for the understanding of fundamental questions related to ophiolite obduction and mountain building processes (e.g., Glennie et al., 1973; Searle, 2019; Searle & Cox, 1999). For example, the well exposed thrust sheets of oceanic crust and upper mantle of the Semail ophiolite have helped decipher the composition of oceanic lithosphere, and investigate how more dense oceanic lithosphere can be emplaced onto more buoyant continental margins (e.g., Pearce et al., 1984; Searle & Malpas, 1980). Metamorphic soles accreted beneath the mantle sequence peridotites, exposed in tectonic windows beneath the ophiolite, have provided important clues for subduction initiation (Rioux et al., 2016). Folded and thrusted granulite facies meta-sedimentary rocks exposed in the Bani Hamid thrust sheet have been key for making inferences on how the lower continental crust deforms, and was buried to depths of ca 30–40 km and then exhumed (Searle et al., 2014, 2015). Unsurprisingly, the Semail ophiolite (Glennie et al., 1973; Lippard et al., 1986), largely considered as the finest example of its kind, has been the focus of numerous petrological, geochemical, thermobarometric, and structural studies (e.g., Ambrose & Searle, 2019; Boudier et al., 1995; McLeod et al., 2013; Rioux et al., 2013, 2016; Searle & Cox., 1999; Searle et al., 2015, 2014; Tilton et al., 1981).

Over the past 50 years or so, geologists have concentrated research on the Semail ophiolite, particularly on its original tectonic setting and processes operating during its emplacement onto the UAE-Oman continental margin. However, there have been only a few geophysical experiments carried out to determine the deep crustal structure, especially the geometry and physical properties of the ophiolite and the crust that underlies it. Extensive hydrocarbon exploration efforts, mainly in the form of shallow reflection profiles, have allowed the sedimentary sequences in the foreland basins (situated to the west of the mountain
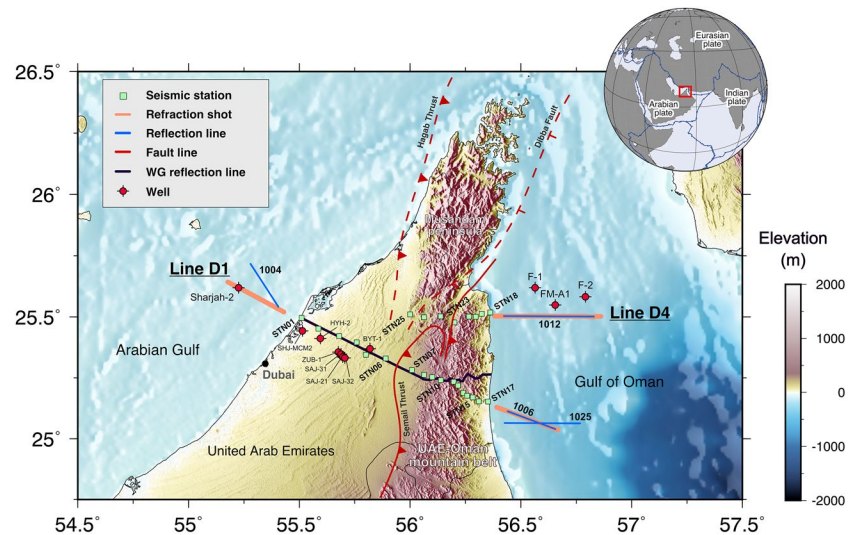
Figure 1. Location map of the study area. Green squares are the broadband seismometers used in the experiment. Stations are progressively counted from west to east along Line D1 (STN01–STN17) and from east to west along Line D4 (STN18–STN25). Colored lines offshore the UAE show multichannel-seismic profiles (blue lines) and wide-angle refraction and reflection profiles (orange lines) acquired by R/V Hawk Explorer. The main tectonic structures are highlighted with red lines. Location of the wells are taken from WesternGeco Report (2005). The inset in the upper-right corner shows the location of the UAE along with the main plate boundaries in blue.

range) to be imaged in detail. In contrast, the deep structure of the UAE-Oman mountain range is less well known due to a lack of deep, high-quality seismic data and the difficulties of imaging beneath a relatively high-velocity and dense ophiolite. Particularly in the relatively less explored eastern offshore, where direct geological observations are not possible, geophysical methods can provide valuable insights into whether the ophiolite is rooted or detached from Tethyan oceanic lithosphere in the Gulf of Oman (Ali et al., 2020).

Previous deep seismic reflection studies have attempted to illuminate the crustal structure of the UAE. On behalf of the Ministry of Energy of the UAE, WesternGeco has acquired four deep seismic profiles: two broadly orthogonal and two parallel (one in the middle of the mountains and another along the axis of the foreland inland) to the mountain range. Interpretations on corresponding time-migrated reflection profiles and further processing by Naville et al. (2010) and Tarapoanca et al. (2010) provide meaningful information on the foreland basin and allochthonous structure. However, sub-ophiolite structure, including the present-day Moho, are not adequately resolved and did not allow any interpretation to be carried out at larger depths.

Great strides have been made with a new interdisciplinary study (Ali et al., 2020), consisting of onshore/offshore active and passive seismic methods, potential field modeling and surface geological mapping. The study of Ali et al. (2020) has been instrumental in probing the crustal structure of the UAE, allowing detailed inferences about ophiolite structure, foreland basins and the lower crust to be made. Although the use of receiver function analysis together with gravity modeling has allowed first-order constraints to be placed on the crustal thickness beneath the transects, limitations of the methods (e.g., due to the presence of thick sedimentary basins, steeply dipping Moho, presence of strong crustal reflectors in the crust) prevented the completion of an accurate depth-to-Moho model. Additionally, there is still uncertainty as to how far the crust of the Arabian passive margin extends into the offshore, and therefore the nature of the crust that underlies the Gulf of Oman.

In this study, we combine active and passive seismic data to reconstruct the crustal structure across two transects orthogonal to the UAE-Oman mountain range. While a number of active seismic profiles have been shown in Ali et al. (2020), namely reflection transect 1012 and refraction transects D1 and D4 (Figure 1), here we present a series of new depth-migrated reflection images from the Gulf of Oman and the

Arabian Gulf, with a more in-depth analysis of the wide-angle seismic profiles. Our new depth-to-Moho estimates are obtained by exploiting a recently developed passive-seismic method (Virtual Deep Seismic Sounding—VDSS), which is capable of producing a well-constrained and substantially improved crustal-thickness model where receiver function has shown significant limitations.

2. Tectonic Setting

Our knowledge about the composition of the Arabian Platform basement (eastern Arabia) has been largely inferred from a few scattered inliers in Oman (Mercolli et al., 2006), and volcanic and sedimentary exotic clasts embedded in intruded salt domes offshore Abu Dhabi (Arabian Gulf), which indicate Ediacaran and Cryogenian ages (Thomas et al., 2015). Despite the extensive lack of basement exposure in eastern Arabia, it is thought that continental growth, possibly via magmatic accretion, has shaped the Arabian Platform architecture (Alessio et al., 2018; Pilia, Hu, et al., 2020; Whitehouse et al., 2016).

In the early Paleozoic, the UAE was located in the southern hemisphere on the northern part of the supercontinent Gondwana, facing the Paleotethys Ocean. From Early Permian to Early Jurassic, the northern Gondwana margin was subject to multiple rifting events (Ali & Watts, 2009). Rifting commenced in the early Permian and by the Middle Permian an extensive carbonate platform was developed along the entire continental margin, with a general absence of magmatic material. A few rift-related alkali basalt sills were intruded into the early Tethyan oceanic domain preserved in the Hawasina and Haybi complexes structurally beneath the Semail ophiolite (Searle, 2007). Middle Triassic-Early Jurassic extension was accompanied by voluminous transitional-tholeiitic volcanism that culminated with the continental breakup of the Cimmerian Terranes, and the formation of the new Neotethyan ocean (Glennie et al., 1973; Searle et al., 1980). While the Cimmerian terranes drifted away from the Arabian margin and were eventually accreted onto Eurasia, seafloor spreading continued in the Neotethys until the Cretaceous, and beyond. From mid-Permian to mid-Cretaceous, the UAE-Oman margin was a mature carbonate-dominated rifted margin. The obduction of the Semail ophiolite from the Tethyan ocean onto the continental margin since Cenomanian time marked the ending of rifting and the onset of compressional tectonics. During the Cenomanian (Tilton et al., 1981), between 96.1 and 95.5 Ma (Rioux et al., 2013), the Semail ophiolite formed at a fast-spreading center above a shallow northeast-dipping subduction zone (Lippard et al., 1986; Pearce et al., 1984; Rioux et al., 2016; Searle & Malpas, 1980). From 95 to 70 Ma, a series of thrust sheets were progressively emplaced from northeast to southwest onto the subsided Arabian passive continental margin (Glennie et al., 1973; Searle & Cox, 1999). The underthrust leading edge of the Arabian continental margin constitutes the melt source of leucogranite dykes that subsequently intruded the wedge of the Semail ophiolite mantle sequence, as observed in the UAE (Rollinson, 2015; Searle et al., 2015). It is possible that following ophiolite emplacement the downgoing Arabian continental margin reached a maximum depth of 80–100 km, as indicated by the presence of eclogites exposed only in the As Sifah region, SE of Muscat (Searle et al., 2004). In the UAE part of the mountain belt, the mantle sequence is also cut by a thrust slice of folded, high-temperature, granulite-amphibolite facies rocks (Bani Hamid) that has been exhumed by an out-of-sequence thrust (Searle et al., 2015). The exhumed Bani Hamid granulite facies rocks suggest that the lower crust of the UAE-Oman mountain range may have a similar composition.

A natural consequence of the emplacement of the ophiolite load was flexure of the pre-existing underlying rifted continental margin and formation of a foreland-type basin, the Aruma basin to the west of the UAE-Oman mountains (Ali & Watts, 2009; Patton & O'Connor, 1988). Thin-skinned deformation dominated the emplacement process, leaving the underlying Mesozoic shelf sediments relatively undeformed. Following the end of the obduction process in the Early Maastrichtian, a deep sedimentary basin also formed to the east of the UAE-Oman mountains in the Gulf of Oman, probably by flexure. A compressive tectonic regime promoted by the opening of the Red Sea, and culminating with continental collision in the Zagros mountains, is affecting the current geological evolution of the region. Early effects of the collision can be seen in the Musandam peninsula, where the Oligocene-early Miocene thrusting along the Hagab thrust records initial crustal thickening.

3. Data and Methods

Multi-Channel Seismic (MCS) reflection and Wide-Angle refraction data were acquired in July 2014 as part of an integrated active and passive seismic, geological mapping and potential field experiment in the UAE (Ali et al., 2020; Pilia et al., 2015; Pilia, Jackson, et al., 2020). The experiment, extending from the Arabian Gulf to the Gulf of Oman, was designed to image the deep-crustal and upper-mantle structure of the north-eastern margin of the Arabian Plate, including the UAE-Oman mountain belt and its foreland basins. The focus here is on two active- and passive-source E-W transects (Line D1 and D4), augmented by a number of depth-migrated reflection lines interpreted using well ties (Figure 1). One profile runs for ca 160 km from the Arabian Gulf to the Gulf of Oman across the Musandam peninsula (Line D1), while another extends for ~80 km from the UAE-mountain belt to the eastern offshore in the Gulf of Oman (Line D4).

Seismic reflection data were acquired using the commercial seismic ship M/V *Hawk Explorer*. Shots from a 5,420 cubic inches (88 liters) air-gun array were fired every 20 s and recorded for 15 s by a 408 channel (1 ms sampling rate), 5-km-long streamer.

A larger source array and greater shot intervals enable high signal-to-noise ratio and deeper travel time picks for wide-angle data. In this case, the source was equipped with four arrays of 12 air guns (7,060 cubic inches, 116 liters) towed at 6 m depth. A total of about 900 air-gun shots were fired offshore (400 for Line D4 and 500 for Line D1 equally distributed between the Arabian Gulf and Gulf of Oman) at 50-s time interval (equal to 90 m—controlled by differential GPS). Air-gun shots were then recorded on land by 25 broadband three-component seismometers. Data quality is variable but generally good, allowing arrival identification up to about 70 km offset.

Land stations used for the active shots offshore were separately operational for a year to record passive seismic data (2015 for Line D4 and 2016 for Line D1).

3.1. Active Source Data Processing

We conducted seismic processing for the reflection lines up to pre-stack time migration using ProMax and Seismic Unix. WesternGeco performed final pre-stack processing and conversion of Two-Way Travel Time data to depth using in-house software. The profiles we present here are pre-stack depth-migrated (Figure 2). The processing flow steps included: Removal of swell noise and seismic interference noise attenuation, frequency-wavenumber filtering in the shot domain, true amplitude recovery (spherical divergence correction and exponential gain correction), deterministic water layer demultiple and radon demultiple, and anisotropic Kirchhoff pre-stack time migration. This was followed by anisotropic reflection tomography and Kirchhoff pre-stack depth migration. In Figure 2 we show examples of the final uninterpreted and interpreted depth-migrated profiles.

Since the land stations were continuously recording during the wide-angle experiment, the exact timing of the air-gun shots was used to cut the seismic records into separate traces of 40 s length, after which we assembled them into receiver gathers. After conversion of the gathers to SEGY format, the processing included the application of: i) frequency filtering using a band-pass Butterworth filter (2-4-13-15 Hz), ii) automatic gain control, iii) a coherency filter to enhance the visibility of different phases and iv) a linear velocity reduction to ease visibility of seismic arrivals, especially those reflected from the Moho discontinuity (Figure 3).

Seismic arrivals are picked by hand on the receiver gathers (unfiltered where possible). We recognized intra-crustal refractions (P1 and P2), possible Moho reflections (PmP) and upper mantle refractions (Pn) from the shots in the Gulf of Oman (see STN 15, STN16, STN19, and STN21 in Figure 3). Upper crustal refractions P3 were recorded from sources located in the Arabian Gulf. Phase identification from the western extension of Line D1 in the Arabian Gulf was considerably harder as the data display relatively poorer quality. This is likely because of the sandy nature of the terrain where seismic sensors were deployed. Indeed, the presence of thick sand dunes significantly alters the seismic signal due to the high impedance contrast between sand dunes and underlying formations, reverberations within the dunes, elastic attenuation and topographic scattering, which ultimately produce seismic records characterized by a low signal-to-noise ratio. Moreover, for environmental reasons, we were not able to use active sources onshore, with the consequence that we
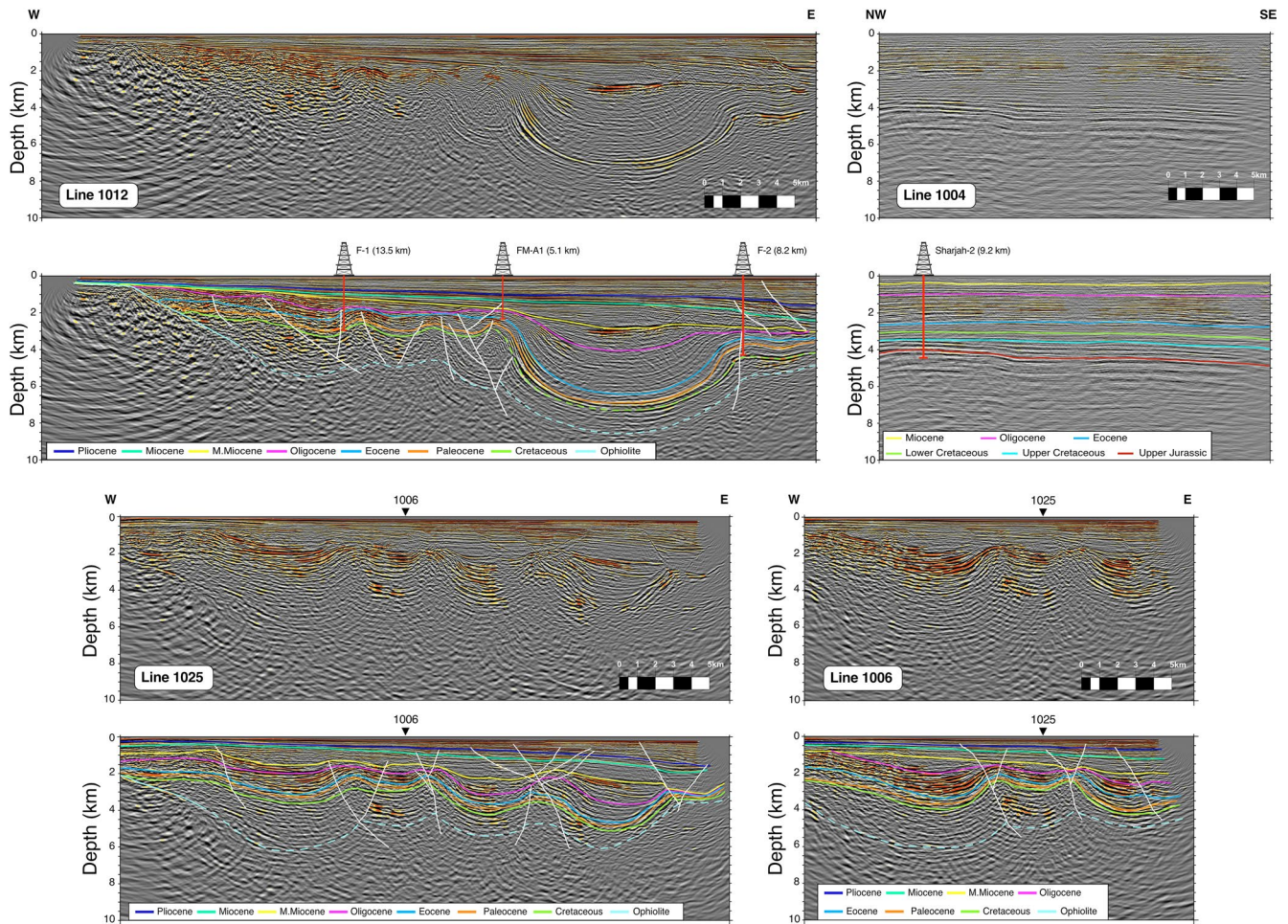
Figure 2. Pre-stack depth-migrated images. Lines 1012 and 1006 are coincident with the eastern offshore portions of Line D4 and D1, respectively. Colored lines mark prominent reflectors and interpreted stratigraphy tied to well F-1, FM-A1 and F-2 (red vertical lines). White lines are interpreted faults (positive flower structure). Colored horizons are dashed where uncertain. Location of the seismic transects is shown in Figure 1.

could not obtain a reversed data set. Despite careful analysis and inspection of the filtered and unfiltered seismic sections, we did not find evidence for lateral continuity of seismic arrivals at STN07 (from air-gun shots in the Arabian Gulf), which is the farthest station that recorded usable data from the Gulf of Oman (see Figure 3). STN24, STN25, and STN14 did not record usable data due to a timing issue with the GPS. Depending on offset, picking uncertainty was assumed to range from 0.05 to 0.1 s for P1 arrivals, 0.10–0.15 for P2 and P3 arrivals, and 0.15 to 0.2 for PmP and Pn.

After assembling the travel-time picks from the receiver gathers, the two-dimensional (2-D) ray tracing software Rayinvr (Zelt & Smith, 1992) was used to model the wide-angle seismic data, following a layer-stripping approach (Zelt, 1999). Additional geological and geophysical constraints were incorporated in the modeling procedure where available.

### 3.2. Passive Source: Virtual Deep Seismic Sounding

Less conventional than wide-angle active-seismic experiments, VDSS is a relatively new approach that uses wide-angle reflections from passive sources (i.e., earthquakes). The method employs the *SsPmp* phase (Figure 4), an incident *S*-wave from epicentral distance between 30° and 50° that reflects under the free surface and converts to *P*-wave, which subsequently reflects off the Moho (Tseng et al., 2009). The *S*-to-*P* under-side reflection is the virtual source for the wide-angle reflection bouncing from the crust-mantle boundary. One of the key advantages of the method is that the *P*-wave reflection from the Moho is post-critical. As such,
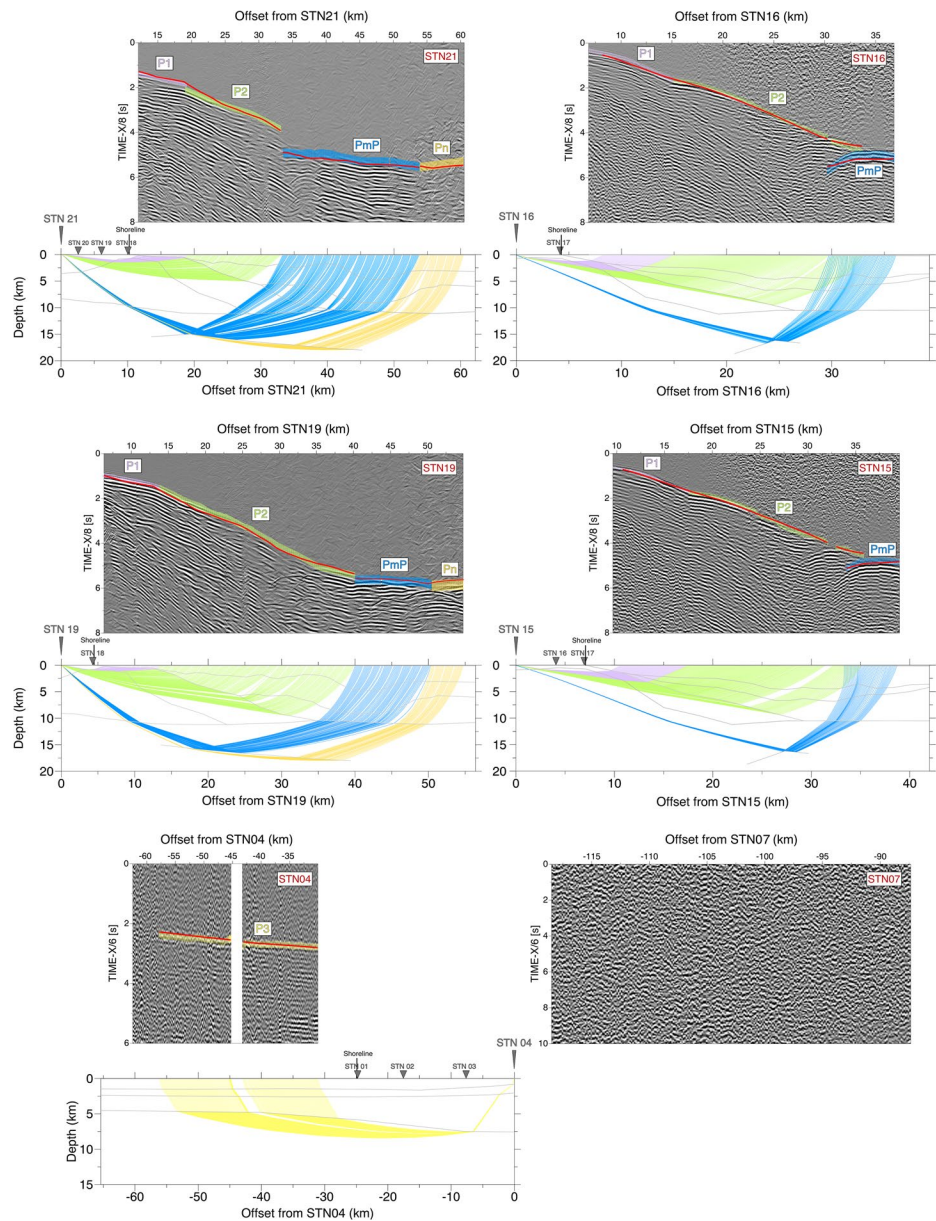
Figure 3. Representative record sections for receiver gathers STN15, STN16, STN19, STN21, STN04, and STN07. Records from STN15 and STN19 have been modified from Ali et al. (2020). Receiver gathers display the identified seismic phases (colored lines) and predicted travel times based on the final model shown in Figure 6 (red dots). Receiver gathers are underlain by corresponding ray path plots. STN07 did not record usable data from the sources located in the Arabian Gulf.

the *SsPmp* phase is characterized by a high signal-to-noise ratio. Additionally, the low frequency content inherent to the method allows to suppress undesired intra-crustal reflections. However, because of the total internal reflection from the Moho, the *SsPmp* phase undergoes a phase shift that varies with epicentral distance when compared to the *Ss* arrival. Furthermore, the *SsPmp* phase is more sensitive to lateral velocity variations than near-vertical phases such as the Ps, due to the large distance between virtual source and receiver (on average ∼100 km).

A proxy for crustal thickness can be calculated from the arrival time of the *SsPmp* phase relative to the incident S wave, as in the following equation:
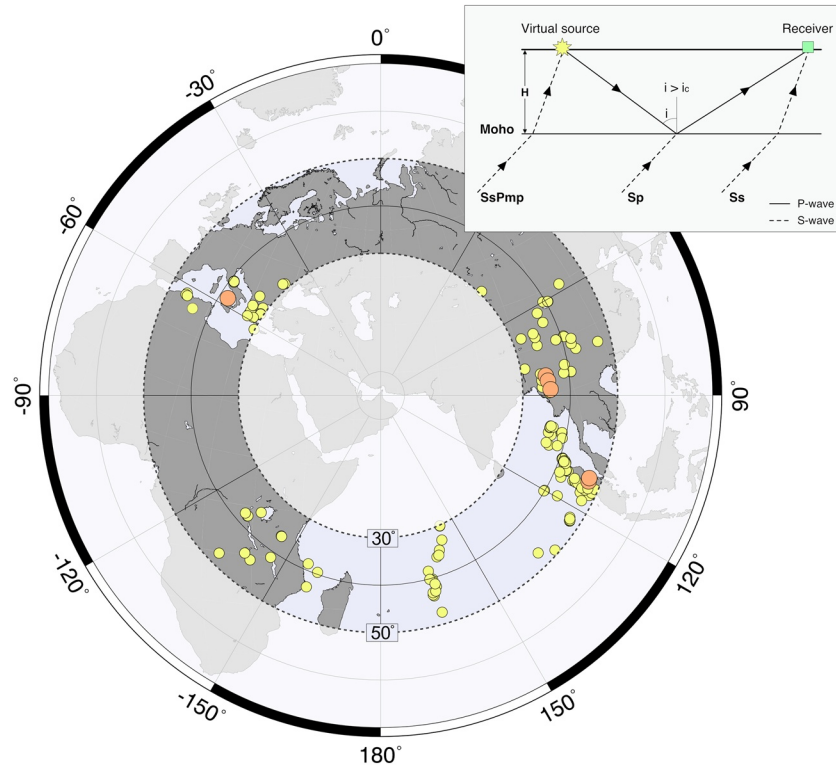
Figure 4. Distribution of passive-seismic sources in the epicentral distance range 30°–50° used to measure the $T_{SsPmp-Ss}$. Yellow and orange dots depict earthquakes with a focal depth smaller and larger than 100 km, respectively. Upper right inset shows a schematic ray diagram of the main phases observed during the analysis of VDSS traces (i is the incident angle at the Moho, i_c is the critical angle).

$$T_{SsPmp-Ss} = 2H \left(V_p^{-2} - p_\beta^2 \right)^{1/2} \tag{1}$$

where H is the crustal thickness, V_p is the average crustal velocity and p_β is the ray parameter, or horizontal slowness, of the incident *S*-wave, determined from the known source-receiver geometry and the ak135 velocity model (Kennett et al., 1995). We now describe the procedure adopted to process the VDSS data set, which is largely based on the implementation proposed by Thompson et al. (2019).

We analyze broadband waveforms collected by the seismic sensors distributed along segments D1 and D4 across the UAE-Oman mountain range and foreland area (Figure 1). We select seismic sources with moment magnitude larger than 5.0 in the epicentral distance range 30°–50°, resulting in a total of 156 earthquakes (Figure 4).

Traces associated with the *S*-arrival time are windowed using predictions from the global reference model ak135 (Kennett et al., 1995). Pre-processing involves removing the instrument response from the event data and apply a second-order zero-phase Butterworth filter with corner frequencies of 0.05 and 0.5 Hz. Horizontal components are then rotated into radial and tangential components. In order to remove source-wavelet effects (e.g., source-side scattering and source time-function complexities) we apply the source normalization method of Yu et al. (2013). This allowed us to account for all seismic events within the *SsPmp* epicentral distance limits, regardless of their focal depths. Therefore, we calculate the angle necessary to rotate the vertical and radial component traces into pseudo-*S* component using the ak135 (see Thompson et al., 2019; Yu et al., 2013). These are then deconvolved from the vertical and radial component VDSS traces using an extended-time multitaper approach (10 s sliding window, 75% window overall, 3 Slepian tapers; Helffrich, 2006). After this step, vertical component VDSS traces are visually inspected and selected if they satisfy three main criteria: i) a prominent *Ss* arrival centered at time zero; ii) evidence of a stable deconvolution
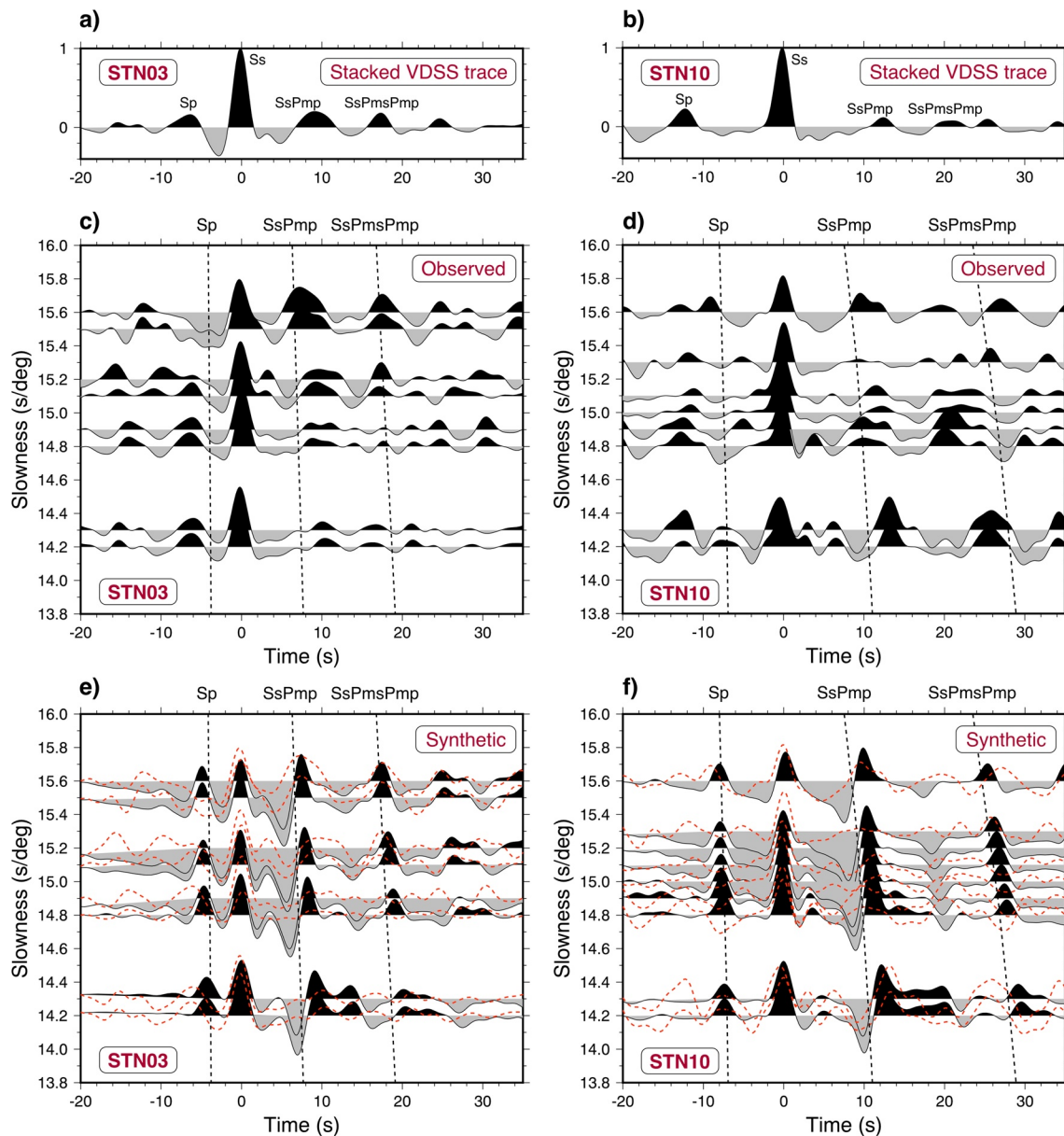
Figure 5. Two examples of observed (c), (d) and synthetic traces (e), (f) for STN03 and STN10. (a) and (b) are obtained by stacking all available VDSS traces for the respective station. Traces are aligned along the *Ss* arrival at time zero. The dashed black lines are the predicted traveltimes for *Sp*, *SsPmp* and *SsPmsPmp* phases, calculated using a modified version of the ak135 velocity model to include the crustal thickness estimated with the 1-D migration procedure. Clear moveout of the *SsPmp* phase is observed across the slowness range, arriving earlier at large slowness (i.e., shorter epicentral distance). Note the larger arrival time of the *SsPmp* phase that characterizes STN10, compatible with a greater crustal thickness. Dashed red lines in (e) and (f) are VDSS observed traces that overly the synthetic seismograms.

(i.e., no ringing or unwarranted oscillatory signal); iii) evidence of a prominent pulse associated with the *SsPmp* arrival time, and those corresponding to the precursory *Sp* and reverberatory *SsPmsPmp* phases. Expected traveltimes and waveforms were computed with the aid of synthetic seismograms constructed using the reflectivity method of Fuchs and Müller (1971). For this endeavor, we assume a mantle half-space and a single crustal layer with thickness below each station based on the seismically and gravimetrically constrained cross-sections in Ali et al. (2020). The effective number of retained VDSS traces was on average higher than 10 per station, with typically around 70% of seismograms removed from our data set to ensure that only high-quality VDSS traces are included in our computations. As a final check, we also compare observed and synthetic seismograms (Figure 5). For each station, observed traces are binned and stacked

by slowness bins of 0.2 s deg^{-1}, allowing a 50% overlap. We illustrate two examples in Figure 5: one for STN03, located in the foreland area where the crust is assumed to be relatively thin, and STN10, located in the mountain belt where $T_{SsPmp-Ss}$, and therefore crustal thickness, is expected to be larger. Arrival times of the *SsPmp* phase appear to be consistent with those estimated using synthetic seismograms, characterized by a clear moveout across the epicentral distance range (or slowness), as observed from the predicted arrival times. It is important to note that that the *Sp* and *SsPmsPmp* arrival times are affected by the Vp/Vs ratio within the crust (see ray diagram in Figure 4), whereas the $T_{SsPmp-Ss}$ (initial *Ss* branch of the *SsPmp* and the direct *Ss* phase will essentially have an identical travel time) is only affected by the *Vp* velocity. This could explain why the precursory and reverberatory phases are slightly off from the arrival time predicted by the synthetic seismograms.

At this stage, solving Equation 1 to calculate crustal thickness is not difficult; however, it is important to have a good knowledge of the bulk velocity V_p. To this end, we make use of insights from other geophysical results to generate an accurate V_p value below each station. In this case, velocities from the wide-angle refraction models are used, although for the vast majority of the stations they constrain the upper and mid crust only. For this reason, lower crustal densities inferred from gravity modeling in Ali et al. (2020) are converted to V_p (Brocher, 2005) to obtain a more complete velocity model of the crust. Finally, the resultant ensemble of depth-migrated one-dimensional (1-D) profiles are linearly stacked to produce a summary trace through which the total crustal thickness can be estimated by determining the depth at which the zero-crossing occurs.

4. Results

### 4.1. Seismic Reflection and Well Data

From the narrow continental shelf of Oman in the south to the Makran Accretionary Prism in the north, the Gulf of Oman is dominated by deep-water sediments of the Sohar basin. Three exploration wells (FM-A1, F-1, and F-2 in Figure 1) were drilled in the late 70s and 80s and are at a relatively short distance from profile 1012 (Figures 1 and 2). Well data from FM-A1, F-1, and F-2 are used for seismic ties to the seismic reflection transects in the Gulf of Oman (Figure 2). They appear to mostly penetrate calcareous siltstone and claystone, calcareous claystone with limestone, and sandstone with minor calcareous claystone derived from the hanging walls and associated footwall uplifts of the Tethyan syn-rift sequence, and erosion of the Arabian margin.

Close to the eastern coastline of the UAE, gently seaward dipping reflectors associated with Pliocene and Middle Miocene strata are observed to a depth of about 500 m, increasing up to 3 km toward the east. Oligocene to Cretaceous units display highly reflective packages, are structurally more complex and onlap a surface with a more chaotic seismic character in the west, which we attribute to the top of the ophiolite sequence. This major boundary (light blue line in Figure 2) steeply deepens seaward and we are able to accurately trace it up to about 5 km depth; farther offshore and at greater depth, seismic horizons are weakly reflective and difficult to identify. Even though it is not possible to recognize distinct reflective events beneath the top of the ophiolite sequence, the full overlying sedimentary package is reasonably well imaged, including a series of possible positive flower structures (white lines in Figure 2), typically associated with strike-slip faults. Some of these faults appear to cut through the Pliocene strata and reach just below the seafloor.

The only seismic reflection transect acquired in the Arabian Gulf is profile 1004. This profile is somewhat poorer in quality than the Gulf of Oman profiles but reveals an extremely simple flat-lying stratigraphy and laterally continuous reflectors. Well Sharjah-2 is located about 10 km to the southwest of the seismic profile and has been used to calibrate the reflectors. A single package of intermittent bright reflectors with relatively high *P*-wave velocity exists between 0.5 and 2.6 km. This defines a layer of Oligocene massive salt.

4.2. Velocity Models

Although we have been unable to image the reflectivity of the lower crust (due probably to our use of a relatively short streamer), layering and thickness of the sediments, as well as the top of the ophiolite inferred
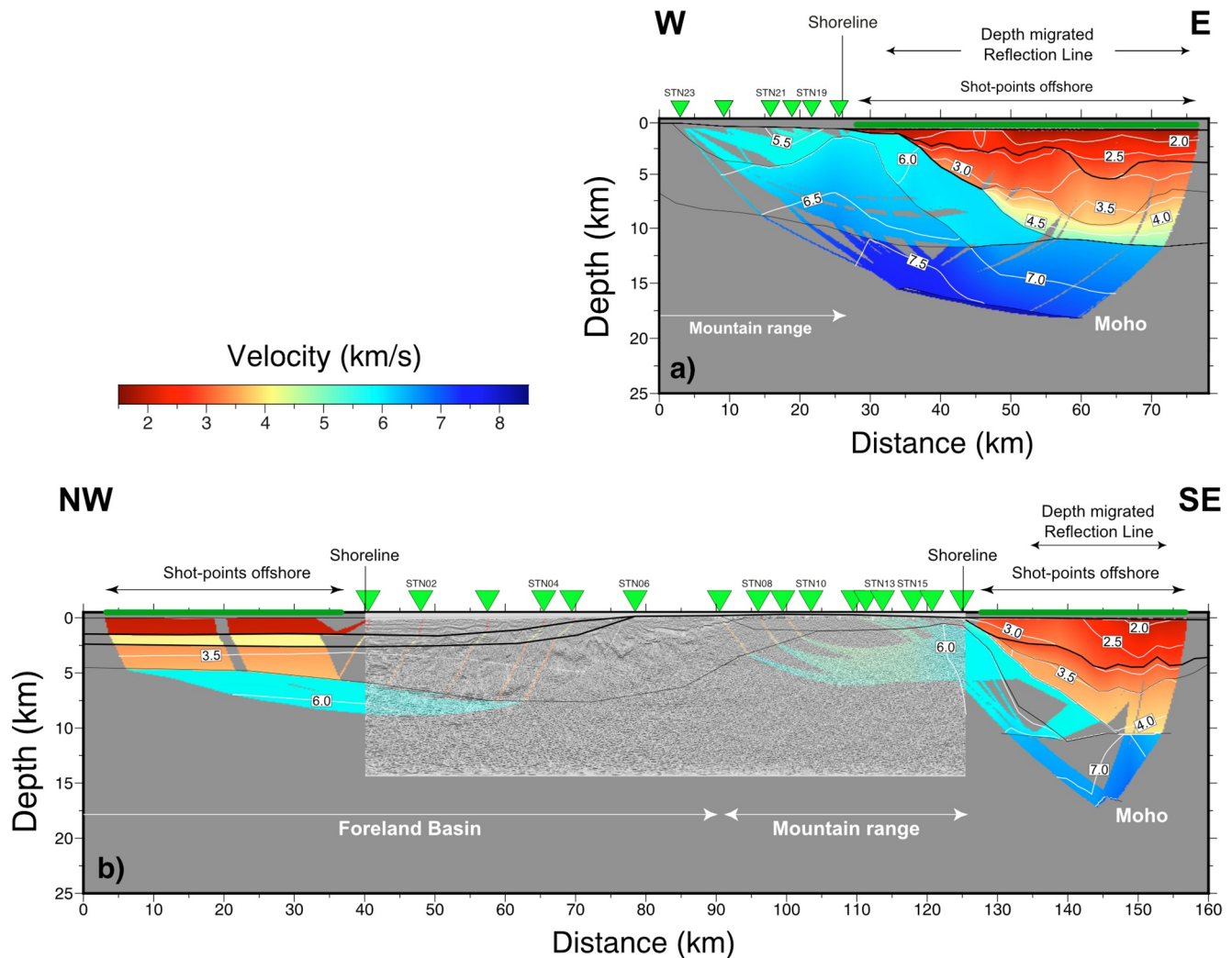
Figure 6. Final *P*-wave velocity model for Line D4 (a) and Line D1 (b). Green inverted triangles show seismic stations and dark-green circles offshore correspond to the shoot points for the wide-angle data. Thin black lines illustrate layer boundaries, while thin white lines are velocity contour intervals (0.5 km s^{-1}). Gray areas are not covered by seismic rays. STN14, STN24, and STN25 did not record usable data. Time migrated reflection line D1 (showed in Figure S1) is added in transparency to enhance imaging at mid-model distances where a gap in the wide-angle seismic data is present. Black thick lines are horizons taken from the reflection images and incorporated during modeling of wide-angle data.

from the seismic reflection images are valuable constraints that can be incorporated while modeling the wide-angle seismic data set. For example, high-resolution water depth, top of the post-obduction Oligocene sediments, and top of the ophiolite body were imaged on seismic reflection profiles in the Gulf of Oman. In addition, thickness and velocity of the uppermost layers (up to ca 5 km depth) in the Arabian Gulf are determined from borehole data of well Sharjah-2 (WesternGeco Report) and were not allowed to change during modeling. Additionally, we integrate in our analysis constraints from the time-migrated reflection line of WesternGeco (Figure S1), specifically the trend of stratigraphic interfaces up to the top of the Jurassic. The final *P*-wave tomographic model was progressively built from top to bottom minimizing the misfit between observed and predicted travel times. We used a total of 2081 and 2207 traveltime picks for Line D4 and D1, respectively (see Table S1 where we also detail the misfit statistics for the two profiles).

Figure 6 illustrates the final 2-D *P*-wave velocity model beneath the UAE-Oman mountain belt and Arabian rifted passive margin. Two distinct domains with different velocity structures appear at approximately both sides of the eastern shoreline from Line D4 and D1. In the eastern regions of the profiles, the upper and mid crust is dominated by a relatively low velocity structure that characterizes the post-ophiolite sediments.

The sedimentary package progressively deepens toward the offshore, reaching a maximum thickness of around 10 km, which is somewhat larger than the depth estimated from the depth-migrated reflection line. Post-ophiolite sediments are marked by seismic velocities that gradually increase from 1.8 km s^{-1} near the seafloor to nearly 4.5 km s^{-1} at the base. This is best observed along Line D4, where a greater number of sources in the offshore allows for relatively better constrained velocity structures (see Figure S2 for rayhits). The sediments are underlain by a relatively thin layer that displays seismic wavespeeds exceeding 4.5 km s^{-1} at 11 km depth. This latter depth marks an interface distinguished by a prominent vertical velocity gradient (velocity increase >1.5 km s^{-1}), which reveals a layer slightly thicker than 6 km with an average velocity of ca 7 km s^{-1}. The base of the eastern offshore domain is defined by clear reflections from an uneven Moho (see Figure 3), which place the Moho at ca 17–18 km depth on both Line D1 and D4. We observe another substantial velocity change in this part of the model with upper mantle seismic velocities rising up to 8.2 km s^{-1}.

A standout feature of the velocity models is the presence of an elongated structure with a distinct velocity in the range 5–6 km s^{-1}, which marks the largest lateral velocity contrast (>3 km s^{-1} in places) with the overburden of Cenozoic sediments in the Gulf of Oman. Between 30 and 60 km model distance of Line D4, the tendency for this high-velocity body is to approach the shoreline with a constant angle of 40°–45° and a nearly constant thickness of ca 5 km. It appears to dramatically thin and crop out in the vicinity of the shoreline where the velocity has decreased by 0.5 km s^{-1}. It marginally thickens again below the mountain belt with a maximum depth of 3.5 km. The crust beneath exhibits gradually increasing velocities but reveals extremely high velocities at the base of the model, particularly along Line D4, where velocities up to 7.6 km s^{-1} are modeled. We interpret the top of the high velocity body as the top of the ophiolite body. The base of the ophiolite is not well resolved seismically, but Moho in Line D4 is gently bulging at middle model distances with laterally homogeneous upper-mantle velocities defined by possible Pn arrivals.

Line D1 is broadly less constrained than Line D4, since it exhibits a considerably less dense ray coverage (Figure S2). As observed from MCS line 1004, the western foreland area is laterally homogeneous with relatively undeformed, sub-horizontal layers. The uppermost layers, which show relatively low wavespeed, overlay a layer of Vp ~6 km s^{-1}, constrained by P3 arrivals and associated to upper Jurassic carbonates, readily identified from the two-way traveltime profile as strong reflectors (Figure S1).

4.3. VDSS Profiles

The differential arrival time between the *SsPmp* and *Ss* phases is in the range 6–11 s, implying significant variations in Moho depth across the profiles. As explain in Section 3.2, VDSS traces have been migrated to depth, with the final crustal thickness profiles shown in Table S2 and Figure 7 (see also Figures S3 and S4 for possible back-azimuthal dependence of the results).

In order to evaluate uncertainties of our crustal thickness measurements, we bootstrap the population of input VDSS traces on a station-by-station basis. We randomly draw 100 samples (allowing repetition) and compute the standard deviation of the bootstrapped samples. Error estimates are typically ±2–3 km, as shown with vertical red bars in Figure 7. However, it is possible that stations with less than 10 VDSS traces (STN15, STN17, and STN19; see Table S2) are not adequately representing the population distribution. Although the bulk velocity V_p used to depth migrate the VDSS traces is relatively well constrained (see Section 3.2), we also investigate the sensitivity of the final crustal thickness to the choice of V_p by depth migrating all traces with sizeable Vp perturbations of ±0.1 km/s, somewhat simulating possible lateral variations of velocity. The results, illustrated as black error bars in Figure 7, indicate that final depth estimates are on average ± 2 km off our best estimate.

The basic trend of the Moho, which appears significantly deeper than the refraction Moho at the west end of Profiles D1 and D4, is to follow the topography. This is most apparent from profile D1, where the westernmost part of the profile exhibits a crust-mantle interface of 30 km, gradually increasing to the east in accordance with rising elevation. Moho depth values sharply rise to the east of the Semail thrust, mimicking the topography, to decrease again until the easternmost stations.
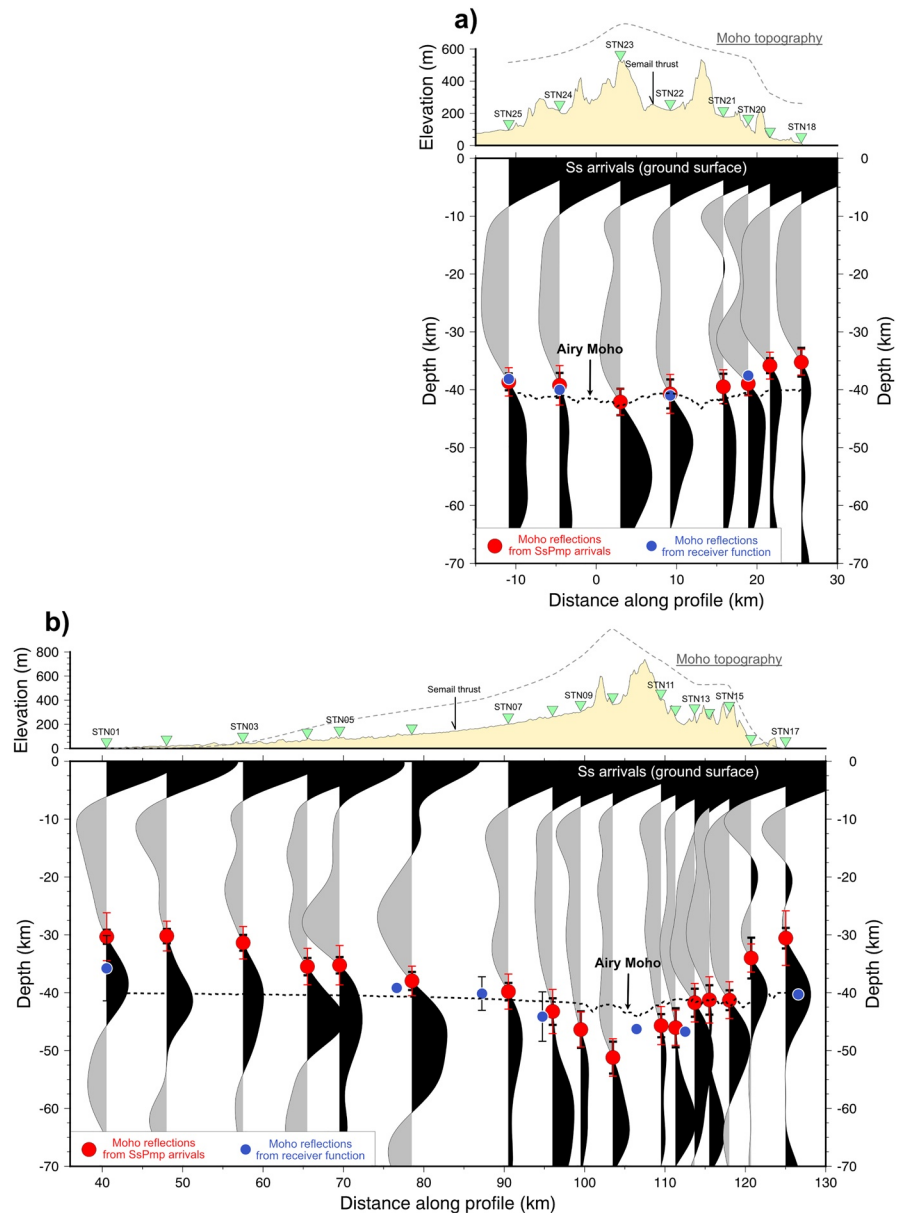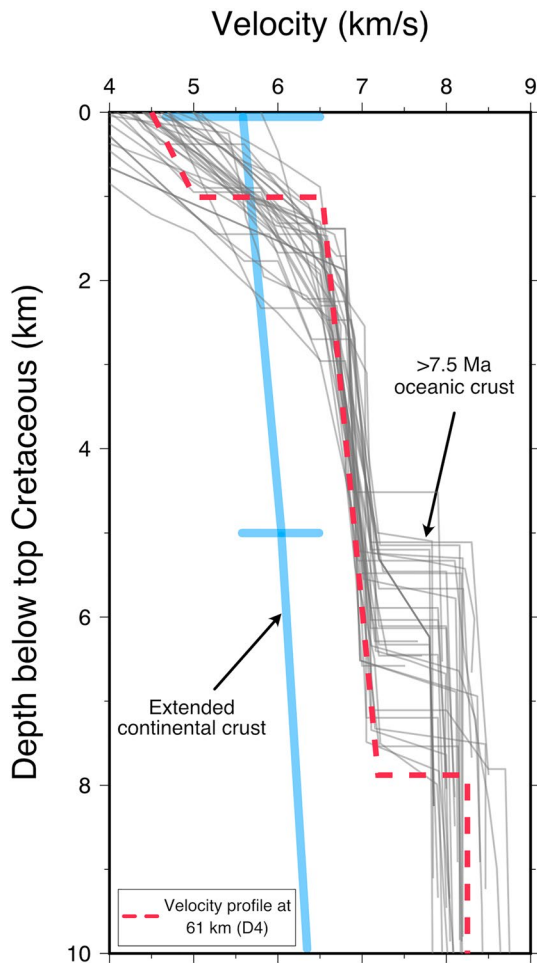
Figure 7. Depth-migrated 1-D reflection profiles constructed using the SsPmp phase. (a) Line D4; (b) Line D1. Red dots are the estimated crustal-thickness values with relative uncertainties obtained through bootstrapping displayed as vertical red bars. Thick, black error bars associated with red dots are uncertainties derived by depth migrating the VDSS traces assuming a ± 0.1 km/s perturbation of the bulk V_p. For comparison, receiver-function-derived crustal depths (Ali et al., 2020) are included as blue dots. Topography is shown above each profile. Black dashed lines show the expected depth-to-Moho assuming an Airy model of isostasy. Gray dashed lines above the topography plots show the smoothed, inverted, seismically constrained Moho to highlight a possible lateral offset between the topographic peak and the crustal root (D1). The offset is not readily visible along Line D4, perhaps due to the fact that our station coverage across the transition from mountain belt to foreland area is more limited.

5. Discussion

5.1. Crustal Structure From Active Seismic Methods

Ravaut et al. (1997), and more recently Ali et al. (2017, 2020), have shown that the UAE-Oman mountain belt is characterized by a N-S trending Bouguer gravity-anomaly high that correlates with the exposed ophiolite. This is flanked on the western side by a gravity low related to the UAE foreland basin. The gravity high
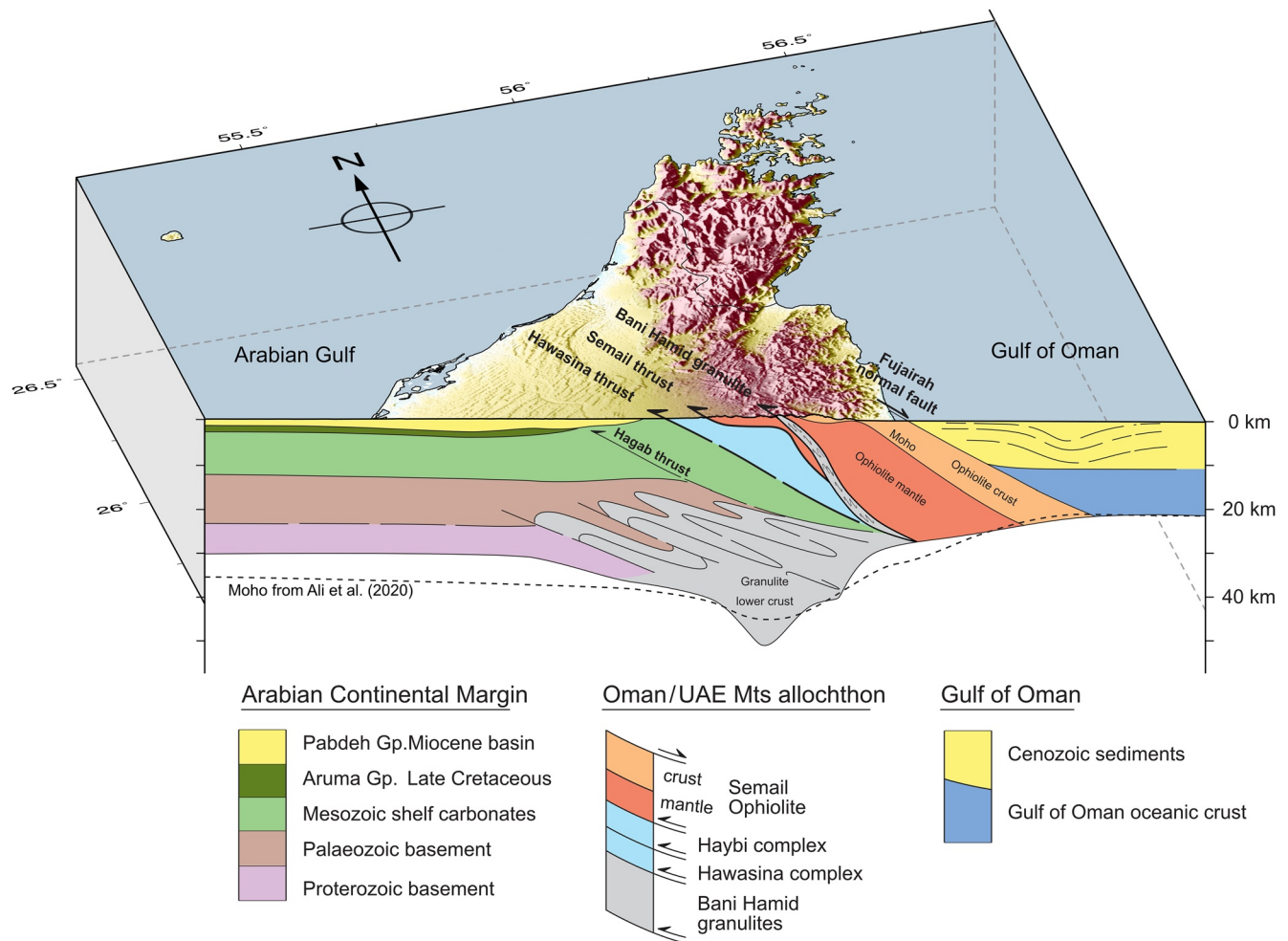
Figure 8. 1-D velocity-depth profile extracted from the final velocity model at model distance 61 km of Line D4 (dashed red line). We compare our velocity profile with the range of typical velocity profiles for "old" oceanic crust formed at fast-spreading centers (gray 1-D profiles), and extended continental crust (light blue line with uncertainties).

extends offshore but does not provide any insight into whether or not the ophiolite is rooted or detached in the Gulf of Oman. In the study of Naville et al. (2010), seismic velocities and thickness of the ophiolite were investigated by using seismic reflection data acquired by WesternGeco along a profile about 20 km south of Line D4. They determine an average velocity of 6 km s^{-1} close to the coast, which decreases to 5 km s^{-1} when about 20 km inland. They also speculate a thickness of the obducted ophiolite of ~5 km when close to the east coast, which landward becomes less than 1 km. Tarapoanca et al. (2010) concentrated on the reflection profile that coincides with the onshore section of Line D4. The aim of their study was to elucidate the crustal architecture in the top 10 km and simulate the kinematic evolution of the obduction process. They present a structural interpretation with the Semail ophiolite as thick as ~5 km near the shoreline, although even in this case picking the bottom reflector of the ophiolite proved to be extremely challenging. More recently, Ali et al. (2020) showed that onshore the western part of the Semail ophiolite is relatively thin, thickening to the east (with a dip of 40°–45°) where it is ~15 km along the coastline, and that it terminates along a NE-dipping normal fault immediately offshore the UAE. They describe the ophiolite as a body with high density, high magnetic susceptibility and high P-wave velocity.

We interpret the high P-wave velocity feature found in the upper crust of the mountain belt and dipping to the east, as the Semail ophiolite. The 5–6 km s^{-1} velocity range is typical of sheeted dikes or upper gabbros from ophiolites in the Troodos, Papua New Guinea, and Newfoundland (Ali et al., 2020). We note that the uppermost section of the oceanic crust (pillow lavas) is not observed anywhere in the UAE, although it is present in Oman (Ambrose & Searle, 2019). Seismic reflection data (Figure 2), with the aid of several wells, allow us to image the stratigraphy of the broad depositional sedimentary basin underlying the Gulf of Oman. The 4.5 km s^{-1} velocity contour of Line D4 may be a good local approximation of the depth to Cretaceous basement.

In agreement with Ali et al. (2020), we associate the surface between the ophiolite and sediment infill as a major east-dipping normal fault that probably marks the eastern extension of the Arabian continental crust. Pilia, Hu, et al. (2020) used relative arrival-time residuals from teleseismic earthquakes to map the three-dimensional lithospheric structure of the region and revealed a lithospheric boundary that runs roughly parallel to the coastline in the immediate offshore. Likewise, they associate the velocity anomaly contrast to the western boundary of oceanic lithosphere. In order to gain insights into the nature of the basement under this locality, in Figure 8 we compare the 1-D velocity depth-profile extracted at model distance 61 km along Line D4 with compilations made for extended continental crust (Christensen & Mooney, 1995) and old (age >7.5 Ma as defined in Christeson et al., 2019) oceanic crust formed at fast-spreading centers (40–80 mm/yr half spreading rate as defined in Christeson et al., 2019). Our profile finds strong affinity of compressional seismic velocities with reported velocities for oceanic crust for this section of the crust, which are substantially higher than average velocities for extended continental crust at comparable depths. One caveat with this result is that seismic velocities in this portion of the model are not accurately reconstructed, as they are only constrained by uni-directional PmP and Pn arrivals. Overall, our results tend to concur with the conclusion postulated by Ali et al. (2020), in that the Gulf of Oman is underlain by oceanic crust, which is bounded to the west by a normal fault now representing the upper (eastern) contact of the Semail ophiolite. This interpretation implies that the normal fault now separates the Arabian continental crust to the west from oceanic lithosphere in the Gulf of Oman to the east, hence the Semail ophiolite may be detached from in-situ oceanic lithosphere in the Gulf of Oman (Figure 9).

Figure 9. Conceptual geological interpretation of a cross section across the UAE-Oman mountains and its bounding sedimentary basins. Our interpretation is consistent with the results obtained in this study and in Ali et al. (2020). Dashed-black line is Moho depth from Ali et al. (2020).

One important inconsistency between our velocity models and the interpretation of Ali et al. (2020), as well as the Moho topography shown in Figure 7, lies at mid-crustal depths beneath the mountains and at the continent-ocean transition region. While we find the Moho to be relatively shallow in the Gulf of Oman, a credible observation, if the gravity effect of relatively low-density Cenozoic sediments is compensated by the relatively high density of a shallower mantle, it is difficult to justify a present-day shallow Moho (ca 15 km) in the region adjacent to the present-day coastline, as suggested by the active source seismic data acquired along Line D4 (Figure 6). Such interpretation would be in stark contrast with evidence provided from potential-field data modeling and crustal-thickness estimates derived from passive-seismic methods, which place the base of the obducted crust and upper mantle at 23 km depth and the present-day Moho at potentially 30 km. Yet, we recognize high-quality wide-angle seismic reflections of large amplitude at most receiver gathers situated in the east, where they exhibit large (>7 km s^{-1}) apparent velocities. Intriguingly, the 7.0 and 7.5 km s^{-1} velocity contours, as well as the Moho seem to approach the coastline from the east with the same angle as the Semail ophiolite. Rather than calling upon a reflector within the oceanic or continental lithosphere itself, one conjecture is that an older Moho associated with the ophiolite thrust-sheet complex may exist.

5.2. On the Crustal Thickness Beneath the UAE-Oman Mountain Belt

Crustal receiver functions computed by Ali et al. (2020) provide key evidence for Moho topography beneath Line D1 and D4. They focus primarily on the conversion of teleseismic *P*-waves to crustal *S*-waves across the

Moho (Pms) and its multiples, using an assumed average crustal velocity of 6.5 km s^{-1} for depth conversion, and H-k stacking. In relatively high-frequency (0.05–4 Hz), conventional receiver function studies, complex tectonic structure promoted by orogenic episodes has the undesirable effect of disguising *P*-to-*S* energy converted at the Moho. Conversely, in VDSS studies, the *P*-to-*P* conversion from the Moho is post-critical (i.e., total internal reflection of the *SsPmp* phase) with a low frequency content that suppresses intra-crustal reflectors. Thus, the advantage is that strong *SsPmp* arrivals can be detected in complex tectonic settings; this enables us to provide robust observational constraints on the overall Moho configuration across both transects (Table S2 and Figure 7), even in regions where receiver function failed to supply reliable results. That said, a comparison of the Moho depth estimates shown here with those produced by Ali et al. (2020) shows good general agreement, although they may have underestimated the maximum crustal root beneath the mountain range by ca 5 km. One reservation to bear in mind when comparing the two sets of results is that the Moho signature is influenced by different structures due to the different ray geometries used for the two methods.

One important result that emerges from this study is the 20 km thickening of the crust (profile D1) that occurs across a limited region beneath the ophiolite, along the mountain belt (~60 km). Interestingly, the most abrupt deflection of the Moho topography appears immediately to the east of the Semail thrust and is slightly offset landward with respect to the highest elevations of the mountain range (Figures 7 and 9). A similar trend has been observed in the Zagros mountains (Paul et al., 2006), where the Moho exhibits a deflection of 25 km in 160 km distance, with the largest crustal thickness measured beneath the lower elevations of the Sanandaj-Sirjan zone. Similarly, Kummerow et al. (2004) revealed a 20 km step in crustal thickness over a distance of 90 km in the eastern Alps. These observations suggest the UAE-Oman mountains are regionally rather than locally compensated at depth.

A way to test the state of isostatic compensation in mountain belts is to compare the seismically constrained crustal thickness directly with predictions from an Airy model. In Figure S5 we show the computed Airy depth-to-Moho using topography data from model SRTM90 (onshore), assuming densities of 1030, 2800, and 3300 kg m^{-3} for water, crust, and mantle, respectively. As a proxy for the unstretched crustal thickness of the Arabian Platform (zero-elevation) we adopt the Moho depth found in Tkalčić et al. (2006) and Kaviani et al. (2020), which place the crustal-mantle interface at 40 km. The depth to the Airy Moho along transects D1 and D4 is shown as a dashed line in Figure 7. The amount of shortening implied by the Airy model for an elevation of 700 meters would be nearly 10%, assuming the densities and zero-elevation crustal thickness described earlier. Figure 7 shows that there is a major departure between the calculated Airy Moho and the observed seismic Moho beneath the mountain belt and in the foreland area. This indicates that the seismically constrained Moho cannot be explained by an Airy model of isostasy. More importantly, the crustal root appears to be laterally offset landward of the topographic peak, suggesting that the difference between the calculated Airy Moho and the seismically constrained Moho is due, at least in part, to flexure of the Arabian rifted margin by ophiolite loading.

To understand the fundamental effects that the obduction process has exerted on the crustal thickness, we consider the thinned, pre-obduction crustal thickness. Ali and Watts (2009) used gravity anomalies, seismic reflection profiles and exploratory wells to find a stretching factor of the crust underlying the UAE $\beta = 1.3$. Using the estimated crustal thickness of 40 km for the Arabian Platform unstretched crust and applying a stretching factor β of 1.3, the crust following extension and prior to the ophiolite emplacement might have been as thick as 30 km (equal to the unstretched crust divided by β), which is congruent with the depth-to-Moho estimates inferred from the westernmost stations of Line D1. Additionally, Ali et al. (2020) predict that a flexural depression of the pre-existing rifted margin due to the ophiolite load by at least 5 km. Taking these factors into account, it is possible that folding and thrusting during obduction of the Semail ophiolite has thickened the crust beneath the mountain belt by about 16 km (current maximum thickness 51 km minus 35 km, which is the thickness of stretched crust plus the load of ophiolite), thereby creating a substantial crustal root beneath the mountains. Evidence for pervasive folding and thrusting of the lower crust beneath the obducted Semail ophiolite is derived from the Bani Hamid thrust sheet in UAE (Figure 9), where a ca 1 km thick unit of tight to isoclinally folded granulite facies meta-carbonates and meta-quartzites has been thrust into the ophiolite mantle sequence by late-stage out-of-sequence thrusting (Searle et al., 2014). These granulite facies rocks have PT conditions of 850 ± 60 °C and 6.3 ± 0.5 kbar and ^{206}Pb/^{238}U zircon dates of

96.1–95.5 Ma (Searle et al., 2015). Geological mapping shows that the lower crust was thickened by tight to isoclinal folding during this period, corresponding to a deeper Moho (see Figure 16 in Searle et al., 2014).

6. Conclusions

A striking feature of our final compressional velocity model is the presence of a relatively high-velocity region (5–6 km s^{-1}) extending from beneath a thick sediment accumulation in the Gulf of Oman to the surface in the UAE-Oman mountain range. We interpret this as evidence of the geometry of the Semail ophiolite (Figure 9). A major, east-dipping normal fault bounds the eastern limit of the ophiolite, as inferred by seismic reflection images, suggesting that the ophiolite may not be rooted in Tethyan oceanic lithosphere. We also show evidence for the presence of oceanic crust in the Gulf of Oman, underlying a thick layer of Cenozoic sediments. Our crustal thickness model, derived using the VDSS method, is consistent with the presence of a significant crustal root beneath the mountains (Figure 9). Folding and thrusting due to emplacement of the Semail ophiolite has possibly thickened the Arabian continental crust by 16 km. We propose that the thick crustal keel beneath the ophiolite is folded and thrusted granulite facies lower crust metamorphic rocks, similar to those seen in the Bani Hamid thrust sheet.

Data Availability Statement

Data acquisition in the UAE was supported by The Petroleum Institute Research Centre Project LTR14011. The data set used in this study is from Pilia, Jackson, et al. (2020).

References

Alessio, B. L., Blades, M. L., Murray, G., Thorpe, B., Collins, A. S., Kelsey, D. E., et al. (2018). Origin and tectonic evolution of the NE basement of Oman: A window into the Neoproterozoic accretionary growth of India? *Geological Magazine*, *155*(5), 1150–1174. https://doi.org/10.1017/S0016756817000061

Ali, M. Y., Fairhead, J. D., Green, C. M., & Noufal, A. (2017). Basement structure of the United Arab Emirates derived from an analysis of regional gravity and aeromagnetic database. *Tectonophysics*, *712–713*, 503–522. https://doi.org/10.1016/j.tecto.2017.06.006

Ali, M. Y., & Watts, A. B. (2009). Subsidence history, gravity anomalies and flexure of the United Arab Emirates (UAE) foreland basin. *GeoArabia*, *14*(2), 17–44.

Ali, M. Y., Watts, A. B., Searle, M. P., Keats, B., Pilia, S., & Ambrose, T. (2020). Geophysical imaging of ophiolite structure in the United Arab Emirates. *Nature Communications*, *11*(1), 1–10. https://doi.org/10.1038/s41467-020-16521-0

Ambrose, T. K., & Searle, M. P. (2019). 3-D structure of the Northern Oman-UAE ophiolite: Widespread, short-lived, suprasubduction zone magmatism. *Tectonics*, *38*, 233–252. https://doi.org/10.1029/2018tc005038

Boudier, F., & Nicolas, A. (1995). Nature of the Moho transition zone in the Oman ophiolite. *Journal of Petrology*, *36*(3), 777. https://doi.org/10.1093/petrology/36.3.777

Brocher, T. M. (2005). Empirical relations between elastic wavespeeds and density in the earth's crust. *Bulletin of the Seismological Society of America*, *95*(6), 2081–2092. https://doi.org/10.1785/0120050077

Christensen, N. I., & Mooney, W. D. (1995). Seismic velocity structure and composition of the continental crust: A global view. *Journal of Geophysical Research*, *100*, 9761–9788. https://doi.org/10.1029/95jb00259

Christeson, G. L., Goff, J. A., & Reece, R. S. (2019). Synthesis of oceanic crustal structure from two-dimensional seismic profiles. *Reviews of Geophysics*, *57*(2), 504–529. https://doi.org/10.1029/2019rg000641

Fuchs, K., & Müller, G. (1971). Computation of synthetic seismograms with the reflectivity method and comparison with observations. *Geophysical Journal International*, *23*(4), 417–433. https://doi.org/10.1111/j.1365-246x.1971.tb01834.x

Glennie, K., Boeuf, M., Clarke, M. H., Moody-Stuart, M., Pilaar, W., & Reinhardt, B. (1973). Late Cretaceous nappes in Oman mountains and their geologic evolution. *AAPG Bulletin*, *57*(1), 5–27.

Helffrich, G. (2006). Extended-time multitaper frequency domain cross-correlation receiver-function estimation. *Bulletin of the Seismological Society of America*, *96*(1), 344–347. https://doi.org/10.1785/0120050098

Kaviani, A., Paul, A., Moradi, A., Mai, P. M., Pilia, S., Boschi, L., et al. (2020). Crustal and uppermost mantle shear wave velocity structure beneath the Middle East from surface wave tomography. *Geophysical Journal International*, *221*(2), 1349–1365. https://doi.org/10.1093/gji/ggaa075

Kennett, B. L. N., Engdahl, E. R., & Buland, R. (1995). Constraints on seismic velocities in the Earth from traveltimes. *Geophysical Journal International*, *122*(1), 108–124. https://doi.org/10.1111/j.1365-246X.1995.tb03540.x

Kummerow, J., Kind, R., Oncken, O., Giese, P., Ryberg, T., Wylegalla, K., et al. (2004). A natural and controlled source seismic profile through the eastern Alps: TRANSALP. *Earth and Planetary Science Letters*, *225*(1–2), 115–129. https://doi.org/10.1016/j.epsl.2004.05.040

Lippard, S. J., Shelton, A. W., & Gass, I. G. (1986). *The ophiolite of northern Oman*. Blackwell Scientific.

McLeod, C. J., Lissenberg, C. J., & Bibby, L. E. (2013). "Moist MORB" axial magmatism in the Oman ophiolite: The evidence against a mid-ocean ridge origin. *Geology*, *41*(4), 459–462. https://doi.org/10.1130/G33904.1

Mercolli, I., Briner, A., Frei, R., Schonberg, R., Nagler, T., Kramers, J., & Peters, T. (2006). Lithostratigraphy and geochronology of the Neoproterozoic crystalline basement of Salalah, Dhofar, Sultanate of Oman. *Precambrian Research*, *145*(3–4), 182–206. https://doi.org/10.1016/j.precamres.2005.12.002

Naville, C., Ancel, M., Andriessen, P., Ricarte, P., & Roure, F. (2010). New constrains on the thickness of the Semail ophiolite in the Northern Emirates. *Arabian Journal of Geosciences*, *3*(4), 459–475. https://doi.org/10.1007/s12517-010-0237-8

Patton, T. L., & O'connor, S. J. (1988). Cretaceous flexural history of northern Oman mountain foredeep, United Arab Emirates. *AAPG Bulletin*, *72*(7), 797–809.

Paul, A., Kaviani, A., Hatzfeld, D., Vergne, J., & Mokhtari, M. (2006). Seismological evidence for crustal-scale thrusting in the Zagros mountain belt (Iran). *Geophysical Journal International*, *166*(1), 227–237. https://doi.org/10.1111/j.1365-246x.2006.02920.x

Pearce, J. A., Lippard, S. J., & Roberts, S. (1984). Characteristics and tectonic significance of supra-subduction zone ophiolites. *Geological Society, London, Special Publications*, *16*(1), 77–94. https://doi.org/10.1144/gsl.sp.1984.016.01.06

Pilia, S., Ali, M., Watts, A., & Searle, M. (2015). UAE-Oman mountains give clues to oceanic crust and mantle rocks. *Eos*, *96*. https://doi.org/10.1029/2015EO040937

Pilia, S., Hu, H., Ali, M. Y., Rawlinson, N., & Ruan, A. (2020). Upper mantle structure of the northeastern Arabian Platform from teleseismic body-wave tomography. *Physics of the Earth and Planetary Interiors*, *307*, 106549. https://doi.org/10.1016/j.pepi.2020.106549

Pilia, S., Jackson, J., Hawkins, R., Kaviani, A., & Ali, M. Y. (2020). The southern Zagros collisional orogen: New insights from transdimensional-trees inversion of seismic noise. *Geophysical Research Letters*, *40*. https://doi.org/10.1029/2019GL086258

Ravaut, P., Bayer, R., Hassani, R., Rousset, D., & Yahya'ey, A. A. (1997). Structure and evolution of the northern Oman margin: Gravity and seismic constraints over the Zagros-Makran-Oman collision zone. *Tectonophysics*, *279*, 253–280. https://doi.org/10.1016/s0040-1951(97)00125-x

Rioux, M., Bowring, S., Kelemen, P., Gordon, S., Miller, R., & Dudás, F. (2013). Tectonic development of the Samail ophiolite: High-precision U-Pb zircon geochronology and Sm-Nd isotopic constraints on crustal growth and emplacement. *Journal of Geophysics Research: Solid Earth*, *118*(5), 2085–2101. https://doi.org/10.1002/jgrb.50139

Rioux, M., Garber, J., Bauer, A., Bowring, S., Searle, M., Kelemen, P., & Hacker, B. (2016). Synchronous formation of the metamorphic sole and igneous crust of the Semail ophiolite: New constraints on the tectonic evolution during ophiolite formation from high-precision U-Pb zircon geochronology. *Earth and Planetary Science Letters*, *451*, 185–195. https://doi.org/10.1016/j.epsl.2016.06.051

Rollinson, H. (2015). Slab and sediment melting during subduction initiation: Granitoid dykes from the mantle section of the Oman ophiolite. *Contributions to Mineralogy and Petrology*, *170*. https://doi.org/10.1007/s00410-015-1177-9

Searle, M., & Cox, J. (1999). Tectonic setting, origin, and obduction of the Oman ophiolite. *The Geological Society of America Bulletin*, *111*(1), 104–122. https://doi.org/10.1130/0016-5147606(1999)111<0104:TSOAOO>2.3.CO;2

Searle, M. P. (2007). Structural geometry, style and timing of deformation in the Hawasina Window, Al Jabal al Akhdar and Saih Hatat culminations, Oman Mountains. *GeoArabia*, *12*(2), 99–130.

Searle, M. P. (2019). *Geology of the Oman mountains, eastern Arabia*. Springer.

Searle, M. P., Cherry, A. G., Ali, M. Y., & Cooper, D. J. W. (2014). Tectonics of the Musandam Peninsula and northern Oman mountains: From ophiolite obduction to continental collision. *GeoArabia*, *19*(2), 135–174.

Searle, M. P., & Malpas, J. (1980). Structure and metamorphism of rocks beneath the Semail ophiolite of Oman and their significance in ophiolite obduction. *Transactions of the Royal Society of Edinburgh: Earth Sciences*, *71*(4), 247–262. https://doi.org/10.1017/s0263593300013614

Searle, M. P., Warren, C. J., Waters, D. J., & Parrish, R. R. (2004). Structural evolution, metamorphism and restoration of the Arabian continental margin, Saih Hatat region, Oman Mountains. *Journal of Structural Geology*, *26*(3), 451–473. https://doi.org/10.1016/j.jsg.2003.08.005

Searle, M. P., Waters, D. J., Garber, J. M., Rioux, M., Cherry, A. G., & Ambrose, T. K. (2015). Structure and metamorphism beneath the obducting Oman ophiolite: Evidence from the Bani Hamid granulites, northern Oman mountains. *Geosphere*, *11*(6), 1812–1836. https://doi.org/10.1130/ges01199.1

Tarapoanca, M., Andriessen, P., Broto, K., Chérel, L., Ellouz-Zimmermann, N., Faure, J.-L., et al. (2010). Forward kinematic modelling of a regional transect in the Northern Emirates using geological and apatite fission track age constraints on paleo-burial history. *Arabian Journal of Geosciences*, *3*(4), 395–411. https://doi.org/10.1007/s12517-010-0213-3

Thomas, R. J., Ellison, R. A., Goodenough, K. M., Roberts, N. M. W., & Allen, P. A. (2015). Salt domes of the UAE and Oman: Probing eastern Arabia. *Precambrian Research*, *256*, 1–16. https://doi.org/10.1016/j.precamres.2014.10.011

Thompson, D. A., Rawlinson, N., & Tkalčić, H. (2019). Testing the limits of virtual deep seismic sounding via new crustal thickness estimates of the Australian continent. *Geophysical Journal International*, *218*(2), 787–800. https://doi.org/10.1093/gji/ggz191

Tilton, G. R., Hopson, C. A., & Wright, J. E. (1981). Uranium-lead isotopic ages of the Samail Ophiolite, Oman, with applications to Tethyan ocean ridge tectonics. *Journal of Geophysical Research*, *86*(B4), 2763–2775. https://doi.org/10.1029/JB086iB04p02763

Tkalčić, H., Pasyanos, M. E., Rodgers, A. J., Gök, R., Walter, W. R., & Al-Amri, A. (2006). A multistep approach for joint modeling of surface wave dispersion and teleseismic receiver functions: Implications for lithospheric structure of the Arabian Peninsula. *Journal of Geophysical Research*, *111*(B11). https://doi.org/10.1029/2005JB004130

Tseng, T. L., Chen, W. P., & Nowack, R. L. (2009). Northward thinning of Tibetan crust revealed by virtual seismic profiles. *Geophysical Research Letters*, *36*(24). https://doi.org/10.1029/2009gl040457

Yu, C.-Q., Chen, W.-P., & van der Hilst, R. D. (2013). Removing source-side scattering for virtual deep seismic sounding (VDSS). *Geophysical Journal International*, *195*(3), 1932–1941. https://doi.org/10.1093/gji/ggt359

WesternGeco Report (2005). *2D structural interpretation of deep seismic reflection profiles in the United Arab Emirates*. WesternGeco.

Whitehouse, M. J., Pease, V., & Al-Khirbash, S. (2016). Neoproterozoic crustal growth at the margin of the East Gondwana continent—age and isotopic constraints from the easternmost inliers of Oman. *International Geology Review*, *58*(16), 2046–2064. https://doi.org/10.1080/00206814.2016.1207207

Zelt, C. A. (1999). Modelling strategies and model assessment for wide-angle seismic traveltime data. *Geophysical Journal International*, *139*(1), 183–204. https://doi.org/10.1046/j.1365-246x.1999.00934.x

Zelt, C. A., & Smith, R. B. (1992). Seismic traveltime inversion for 2-D crustal velocity structure. *Geophysical Journal International*, *108*(1), 16–34. https://doi.org/10.1111/j.1365-246x.1992.tb00836.x